

Article

# Four-Dimensional Thermal Analysis of 888 nm Pumped Nd:YVO<sub>4</sub> Dual-Rod Acousto-Optic Q-Switched Laser

Yijie Shen <sup>†</sup>, Wenqi Zhang <sup>†</sup>, Mali Gong <sup>\*</sup>, Yuan Meng, Yunbin Wang and Xing Fu

State Key Laboratory of Precision Measurement Technology and Instruments, Department of Precision Instrument, Tsinghua University, Beijing 100084, China; shenyj15@mails.tsinghua.edu.cn (Y.S.); zhangwenqi11@163.com (W.Z.); mengy16@mails.tsinghua.edu.cn (Y.M.); binjiu2009@163.com (Y.W.); fuxing@mail.tsinghua.edu.cn (X.F.)

\* Correspondence: gongml@mail.tsinghua.edu.cn; Tel.: +86-138-0120-9391

<sup>†</sup> These authors contributed equally to this work.

Academic Editor: Vincenzo Spagnolo

Received: 14 March 2017; Accepted: 27 April 2017; Published: 8 May 2017

**Abstract:** A theoretical analysis upon the four-dimensional (4D) spatio-temporal temperature dependent dynamics of 888 nm pumped Nd:YVO<sub>4</sub> dual-rod laser is established, which is valid in both continuous-wave (CW) and acousto-optic (AO) Q-switched pulse lasers conditions. Our model can accurately solve the 4D thermal generation and temperature evolution not only in the steady Q-switched state, but also in the first few unstable giant or dwarf pulses region. Factors including ground state depletion (GSD), energy transfer upconversion (ETU), fluorescence branching ratios, temperature-dependent cross sections and nonradiative relaxations processes are comprehensively considered for precisely estimating thermal effects, valid in both the steady pulse region and the unstable region at the beginning. Moreover, temporal and spatial temperature profiles and their coupling effect on output properties at different repetition-rates are discussed. Experiments of high-power high-repetition-rate 888 nm end-pumped Nd:YVO<sub>4</sub> dual-rod CW and AO Q-switched lasers are also firstly presented and the experimental results enjoy good consistency with our theory.

**Keywords:** solid-state lasers; dual-rod lasers; neodymium doped lasers; actively Q-switched lasers; thermal effects

## 1. Introduction

As a new generation of in-band pumped neodymium lasers with a low-quantum-defect, 888 nm pumped Nd:YVO<sub>4</sub> lasers have drawn much attention ever since it was first reported in 2006 [1], with its first high-power high-efficiency Master Oscillator Power-Amplifier (MOPA) system built in 2007 [2]. Nd:YVO<sub>4</sub> enjoys large absorption and stimulated emission cross sections that may easily lead to high gain but weak thermal property due to the low thermal conductivity and high energy transfer upconversion (ETU) coefficient. In addition, an 888 nm pumping scheme is an effective way to compensate thermal effect for output properties upgrading in Nd:YVO<sub>4</sub> laser, which has been widely used in Q-switched [3], mode-locked [4,5] oscillators, pulse amplifiers [6,7] and optical parametric technology [8]. In particular, high-power Q-switched neodymium pulse lasers are widely used in laser machining manufacture [9] and the thermal effect is a key factor. Thus, it is significant to make a complete thermal analysis model in the 888 nm pumped Nd:YVO<sub>4</sub> high-power Q-switched pulse laser.

The upper level lifetime of Nd:YVO<sub>4</sub> is much shorter than that of Nd:YAG [10], which may limit the energy extraction in a Q-switched laser. Using dual-rod or multi-rod is an effective way to upgrade output power in a solid-state laser [11,12]. In 2010, Yan et al. [13] used a dual-rod scheme in acousto-optic Q-switched 808 nm pumped Nd:YVO<sub>4</sub> and Nd:YAG lasers and made the comparative

investigation. The same group [14] used two thermally bonded composite  $\text{YVO}_4\text{-Nd:YVO}_4\text{-YVO}_4$  rod crystals to reduce the thermal effect in their dual-rod Q-switched laser and obtained a 650 kHz repetition rate 73.2 W average power  $\text{TEM}_{00}$ . However, a four-level-system 808 nm pumping scheme has more serious thermal effects than in-band 888 nm pumping [6], and thermally bonded composite crystals are difficult to obtain; thus, Yan's system can be further optimized. Thus, it is significant to make a comprehensive thermal analysis and a numerical simulation model in 888 nm pumped Nd:YVO<sub>4</sub> Q-switched pulse lasers for instructing output property upgrade. There are already several works about thermal analysis for Q-switched lasers. In 2000, Jie Song et al. [15] made a thermal analysis in a passively Q-switched diode-pumped Nd:YAG/Cr<sup>4+</sup>:YAG laser, but they only discussed the thermal lens effect in a steady state. In 2013, Shuaiyi Zhang et al. [16] improved the model for passively Q-switched lasers that can make four-dimensional (4D) space-time-dependent thermal analysis. In 2015, Shixia Li et al. [17] used composite Nd:YVO<sub>4</sub> crystals in their passively Q-switched laser to improve laser performance and developed the theoretical model. For actively Q-switched or pulse pumped lasers, in contrast to a passive case, it is a challenge to simulate and discuss the repetition-rate-dependent properties. In 2009, S. Wang et al. [18] made a detailed 4D thermal analysis for their 946 nm in-band pulse pumped Nd:YAG laser. In 2010, Tao Li et al. [19] built a thermal model for actively Q-switched lasers, and they solved and discussed the time-dependent transient temperature profiles. In 2015, Chen et al. [20] made a 4D thermal effects analysis in a pulsed pumped composite Tm:YAG laser at a low-repetition-rate. However, all of these previous 4D thermal analysis models roughly expressed the thermal load as a certain periodic function. This assumption make these models fail to describe the dynamic heat generation evolution in the first few unstable pulses region. Actually, thermal load in Q-switched lasers is also coupled with complex 4D physical effects like ground state depletion (GSD) [21], fluorescence branching, energy transfer upconversion (ETU) [22,23], cross relaxation (CR) and temperature-dependent cross sections [23,24]. Recently, our group developed the spatial dynamic thermal iteration (SDTI) model [23], which can calculate the 3D thermal load distributions by precisely solving nonradiative transitions using the temperature iteration method. However, the temperature-dependent and repetition-rate-dependent 4D thermal analyses including all of these complex physical processes for actively Q-switched lasers have not been developed.

In this paper, we develop powerful 4D dynamics and a thermal model for multi-rod actively Q-switched laser, and we present the experiment of a high-power high-repetition-rate 888 nm in-band pumped Nd:YVO<sub>4</sub> dual-rod acousto-optic Q-switched laser. In our model, we particularly considered the nonradiative transitions rates, fluorescent branching ratios of each energy manifolds and the ETU process contributing to heat generation. The 4D heat generation in crystal is solved by coupled dynamic equations based on the principles of nonradiative transitions and energy levels dynamics. Temperature-dependent thermal conductivity, absorption and emission cross sections, and their effects on output properties are also included for solving the transient temperature, power, and population distributions. Additionally, the anisotropy of gain medium is considered in our heat conduction equation. Thus, our model can precisely simulate the 4D heat generation evolution in not only the steady pulse region but also the unstable region at the beginning. The simulation results are in good agreement with our measured output data and temperature at various repetition-rates and pump powers in our experiment. To the best of our knowledge, it is the first experimental demonstration of 888 nm pumped multi-rod Q-switched laser oscillator.

## 2. Theoretical Model

### 2.1. AO Q-Switched Laser Dynamics

The energy levels and manifolds for trivalent neodymium in Nd:YVO<sub>4</sub> noted by corresponding wave numbers are depicted in Figure 1. In the Nd:YVO<sub>4</sub> 888 nm in-band pumping scheme, the ions in  $Z_2$  sublevel of ground state manifold  $^4I_{9/2}$  are directly pumped to the laser upper level that  $R_1$  sublevel of manifold  $^4F_{3/2}$  and lasing at 1064 nm, which is usually analyzed as a quasi-three-level system.

According to our previous work [23], the rate equations including GSD, ETU, CR and fluorescence branching ratio are established as:

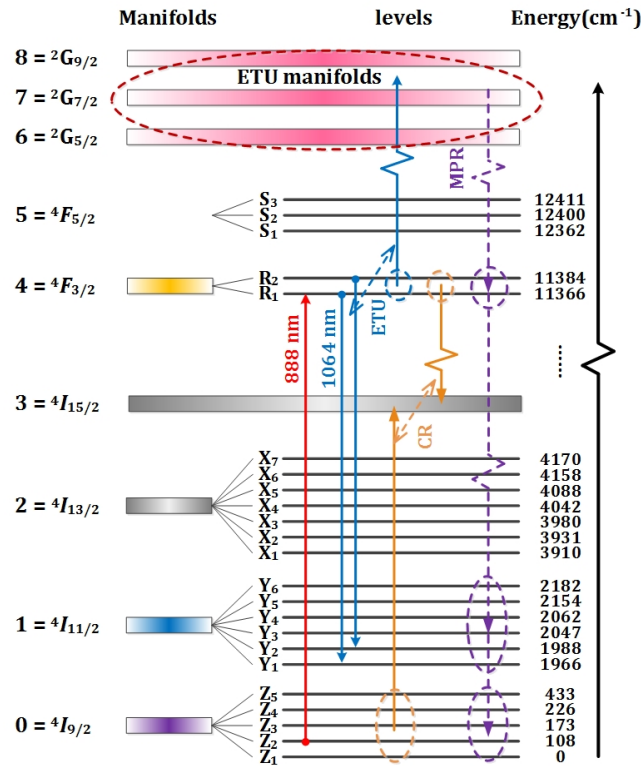


Figure 1. Energy sublevels and main transitions of Nd<sup>3+</sup> ions doped in YVO<sub>4</sub> crystal.

$$\frac{dn_{up}(r, t)}{dt} = W_{up}n_4^2(r, t) - \frac{n_{up}(r, t)}{\tau_{up}}, \quad (1)$$

$$\begin{aligned} \frac{dn_4(r, t)}{dt} = & R_p(r, t)n_0(r, t) - \frac{n_4(r, t)}{\tau_4} - \frac{n_{up}(r, t)}{\tau_{up}} - 2W_{up}n_4^2(r, t) - W_{cr}n_0(r, t)n_4(r, t) \\ & - W_{41}(r, t)n_4(r, t) + W_{14}(r, t)n_1(r, t), \end{aligned} \quad (2)$$

$$\frac{dn_3(r, t)}{dt} = \beta_{43} \frac{n_4(r, t)}{\tau_4} - \frac{n_3(r, t)}{\tau_3} + 2W_{cr}n_0(r, t)n_4(r, t), \quad (3)$$

$$\frac{dn_2(r, t)}{dt} = \beta_{42} \frac{n_4(r, t)}{\tau_4} + \frac{n_3(r, t)}{\tau_3} - \frac{n_2(r, t)}{\tau_2}, \quad (4)$$

$$\begin{aligned} \frac{dn_1(r, t)}{dt} = & \beta_{41} \frac{n_4(r, t)}{\tau_4} + \frac{n_2(r, t)}{\tau_2} - \frac{n_1(r, t)}{\tau_1} + W_{up}n_4^2(r, t) \\ & + W_{41}(r, t)n_4(r, t) - W_{14}(r, t)n_1(r, t), \end{aligned} \quad (5)$$

$$\frac{dn_0(r, t)}{dt} = \beta_{40} \frac{n_4(r, t)}{\tau_4} + \frac{n_1(r, t)}{\tau_1} - R_p(r, t)n_0(r, t) - W_{cr}n_0(r, t)n_4(r, t), \quad (6)$$

where  $r = (x, y, z)$  is the position vector in laser crystal,  $t$  is time,  $n_i$  and  $\tau_i$  ( $i = 0, 1, 2, 3, 4$ ) are the population density and the lifetime of the lowest five manifolds, respectively.  $n_{up}$  and  $\tau_{up}$  are the population density and lifetime of ETU manifolds, respectively.  $\beta_{4i}$  ( $i = 0, 1, 2, 3$ ) is the fluorescent branching ratios from the fourth manifold to the  $i$ -th manifold,  $R_p$  is the pumping rate,  $W_{up}$  is the upconversion coefficient,  $W_{cr}$  is the cross relaxation coefficient, and  $W_{41}$  ( $W_{14}$ ) are stimulated radiation (absorption) rate. The total density of Nd<sup>3+</sup> ions  $n_{tot} = n_0 + n_1 + n_2 + n_3 + n_4 + n_{up}$ . For each energy manifold lifetime  $\tau_i$ , we have [24],

$$\frac{1}{\tau_i} = \frac{1}{\tau_{i,sp}} + \frac{1}{\tau_{i,nr}}, \tag{7}$$

where  $\tau_{i,sp}$  ( $\tau_{i,nr}$ ) is the spontaneous radiation (nonradiative) transition lifetime of the  $i$ -th manifold, and the total transition rate is equal to the sum of spontaneous radiation rate and nonradiative transition rate. According to Einstein's theory of stimulated emission,  $W_{41} = W_{14} = W_s$ .  $R_p$  and  $W_s$  are given by:

$$R_p(\mathbf{r}, t) = \frac{\sigma_{ap}(\mathbf{r}, t)}{h\nu_p} [I_p^+(\mathbf{r}, t) + I_p^-(\mathbf{r}, t)] = \frac{c}{n_c} \sigma_{ap} [\phi_p^+(\mathbf{r}, t) + \phi_p^-(\mathbf{r}, t)], \tag{8}$$

$$W_s(\mathbf{r}, t) = \frac{\sigma_{es}(\mathbf{r}, t)}{h\nu_p} [I_s^+(\mathbf{r}, t) + I_s^-(\mathbf{r}, t)] = \frac{c}{n_c} \sigma_{ap} [\phi_s^+(\mathbf{r}, t) + \phi_s^-(\mathbf{r}, t)], \tag{9}$$

where  $c$  is the speed of light in vacuum,  $h$  is the Planck constant,  $\sigma_{ap}$  ( $\sigma_{es}$ ) is the effective absorption (emission) cross section of pump light,  $\nu_p$  ( $\nu_s$ ) is the frequency of pump light (laser) that is equal to  $c/\lambda_p$  ( $c/\lambda_s$ ),  $I_p^+$  ( $I_p^-$ ) is the intensity of forward (backward) propagating pump light,  $I_s^+$  ( $I_s^-$ ) is the intensity of forward (backward) propagating laser, and  $n_c$  is refractive index of gain medium. For a-cut uniaxial crystal Nd:YVO<sub>4</sub> used in this work, the tiny difference of refractive indexes of ordinary light and extraordinary light can be neglected, thus we regard  $n_c = (n_o + n_e)/2$  approximately. The spatial and temporal distributions of  $\sigma_{ap}$  and  $\sigma_{es}$  are nonuniform due to the influences of the temperature and heat generation distributions and the relationship has been detailedly studied in our previous work, the SDTI model [23]. The cavity, gain medium geometry and the corresponding coordinate frames are depicted in Figure 2. Supposing that the propagation direction of the laser and pump beam is the  $z$ -axis direction, the conversion relations among intensity  $I_s^\pm$  ( $I_p^\pm$ ), photon density  $\phi_s^\pm$  ( $\phi_p^\pm$ ), and power  $P_s^\pm$  ( $P_p^\pm$ ) along the propagation direction can be obtained as:

$$I_s^\pm(z, t) = \frac{c}{n_c} \nu_s \phi_s^\pm(z, t) = \frac{P_s^\pm(z, t)}{\pi \omega^2(z)}, \tag{10}$$

$$I_p^\pm(z, t) = \frac{c}{n_c} \nu_p \phi_p^\pm(z, t) = \frac{P_p^\pm(z, t)}{\pi \omega_p^\pm(z)}, \tag{11}$$

where  $\omega_p^+$  ( $\omega_p^-$ ) is the radius of forward (backward) pump beam, and  $\omega$  is the radius of laser beam. The distributions of pump and laser beams has been studied in previous work [14,23]. In the gain medium, the coupled rate equations for laser and pump photon density propagation are given by:

$$\frac{n_c}{c} \frac{d\phi_s^\pm(\mathbf{r}, t)}{dt} \pm \frac{\phi_s^\pm(\mathbf{r}, t)}{dz} = \sigma_{es}(\mathbf{r}, t) \Delta n(\mathbf{r}, t) \phi_s^\pm(\mathbf{r}, t) + S\beta_{41} \frac{n_4(\mathbf{r}, t)}{\tau_{4,sp}(\mathbf{r}, t)}, \tag{12}$$

$$\frac{n_c}{c} \frac{d\phi_p^\pm(\mathbf{r}, t)}{dt} \pm \frac{\phi_p^\pm(\mathbf{r}, t)}{dz} = \sigma_{ab}(\mathbf{r}, t) \Delta n(\mathbf{r}, t) \phi_p^\pm(\mathbf{r}, t) + S\beta_{40} \frac{n_4(\mathbf{r}, t)}{\tau_{4,sp}(\mathbf{r}, t)}, \tag{13}$$

where  $S$  is the rate at which spontaneous emission is added to the laser emission and population inversion  $\Delta n = n_4 - n_1$ . The value of  $S$  is a very tiny at about  $10^{-11}$  order in this system according to previous research [22]. Equations (12) and (13) are used for solving the power distributions in crystals. Actually, the speed of light is much larger than the speed of producing a Q-switched pulse. The intracavity photon density can be defined as  $\phi_s(t) = \iiint \phi_s^+(\mathbf{r}, t) + \phi_s^-(\mathbf{r}, t) dV / V_m$ , where volume differential  $dV = dx dy dz$  and the mode volume  $V_m = \int_0^l \pi \omega^2(z) dz$ . Thus, we use the rate equation for the intracavity laser photon density to solve the output power, which is given by [22]:

$$\frac{d\phi_s(t)}{dt} = 2 \frac{l_c}{l_{eff}} \left[ S\beta_{41} \frac{n_4(t)}{\tau_{4,sp}} + \frac{c}{n_c} \sigma_{es}(t) \Delta n(t) \phi_s(t) \right] - \frac{\phi_s(t)}{\tau_r} \left[ L + \ln \frac{1}{1 - T_{oc}} + \delta_m(t) \right], \tag{14}$$

where  $l_c$  is the length of each laser crystal, the total length of gain medium in cavity should be  $2l_c$  because of the dual-rod scheme studied in this work,  $l_{\text{eff}}$  is the effective cavity length,  $\tau_r = 2l_{\text{eff}}/l_c$  is the round-trip transit time of light in the resonator,  $L$  is the intrinsic diffraction loss,  $T_{\text{oc}}$  is the transmittance of laser output coupling mirror, and  $\delta_m$  is the loss devoted by the acoustic optical modulator (AOM).  $\Delta n$  here is defined as the spatial average of the population inversion for both crystals. For the investigated dual-rod AO Q-switched laser resonator with two identical laser crystals,  $l_{\text{eff}} = l + 2l_c(n_c - 1) + l_m(n_m - 1)$ , where  $l_m$  and  $n_m$  is the length and refractive index of AOM, and  $l$  is cavity length. The pump intensity can be seen as steady state, because the pump light is continuous-wave high-power in this work. According to Ref. [25], the loss function of AOM is

$$\delta_m(t) = \begin{cases} \delta_0, & (n-1)T \leq t < (n-1)T + t_{\text{on}}, \\ \delta_0 \exp\left[-\left(\frac{t}{t_s}\right)^2\right], & (n-1)T + t_{\text{on}} \leq t < nT, \end{cases} \quad (15)$$

where  $T$  is the period of Q-switch,  $\delta_0$  is the running ultrasonic wave diffraction loss of AOM,  $t_{\text{on}}$  is the running time of AOM in each period and  $t_s$  is the intrinsic turnoff time of AOM. Actually, this function ignores the short process of loss variation at the beginning in each period, i.e., a step point at  $t = (n-1)T$ , which barely affects the pulse producing process. The output laser power is given by:

$$P_s(t) = \frac{h\nu_s\phi_s(t)V_m}{\tau_r} \ln\left(\frac{1}{1-T_{\text{oc}}}\right). \quad (16)$$

### 2.2. Thermal Analysis

The heat generation in laser crystal is caused by the total nonradiative transition processes, in which the power of photon is transformed into heat by multi-phonon relaxations [22,24]. For precisely calculating spatial and transient heat generation, the coupled rate equations and heat conduction equation must be solved. The total thermal power density is the sum of products of energy gap between each pair of manifolds multiplying the corresponding nonradiative transition rate, that:

$$Q(\mathbf{r}, t) = \sum_i \sum_{j < i} \Delta E_{ij} \beta_{ij} \frac{n_i(\mathbf{r}, t)}{\tau_{i,\text{nr}}} = \sum_i \sum_{j < i} hc (\tilde{\lambda}_i - \tilde{\lambda}_j) \beta_{ij} \frac{n_i(\mathbf{r}, t)}{\tau_{i,\text{nr}}}, \quad (17)$$

where  $\Delta E_{ij}$  is the energy gap between manifolds  $i$  and  $j$ . The energy of each manifold here is in the form of wavenumber,  $\tilde{\lambda} = 1/\lambda$ . In the Nd:YVO<sub>4</sub> 888 nm in-band pumped scheme, the heat generation is mainly due to the decays from <sup>4</sup>I<sub>11/2</sub> and ETU manifolds, nearly all of which are nonradiative transitions [6,22]. The ETU induced downward transition is mainly to the <sup>4</sup>I<sub>11/2</sub> manifold and the CR effect is much weaker than ETU so that the CR can be neglected here [20,22,26]. Thus, the thermal power density distribution can be simplified as:

$$Q(\mathbf{r}, t) = hc (\tilde{\lambda}_1 - \tilde{\lambda}_0) \frac{n_1(\mathbf{r}, t)}{\tau_1} + hc (\tilde{\lambda}_4 - \tilde{\lambda}_1) \frac{n_{\text{up}}(\mathbf{r}, t)}{\tau_{\text{up}}} + hc (\tilde{\lambda}_4 - \tilde{\lambda}_f) \frac{n_4(\mathbf{r}, t)}{\tau_4}, \quad (18)$$

where  $\lambda_f$  is the average fluorescence wavelength. For anisotropy medium, the thermal conductivity is a tensor and we also considered temperature-dependent thermal conductivity; thus, the heat conduction equation is given by:

$$\rho C_p \frac{\partial T(\mathbf{r}, t)}{\partial t} - \nabla \cdot \left( \begin{bmatrix} K_x(\mathbf{r}, t) & 0 & 0 \\ 0 & K_y(\mathbf{r}, t) & 0 \\ 0 & 0 & K_z(\mathbf{r}, t) \end{bmatrix} \cdot \nabla T(\mathbf{r}, t) \right) = Q(\mathbf{r}, t), \quad (19)$$

where  $\rho$  is the density of the medium,  $C_p$  is the specific heat capacity of the medium, and  $K_x$ ,  $K_y$ ,  $K_z$  are the thermal conductivity along the three orthogonal principle axes. As for a-cut uniaxial

crystal Nd:YVO<sub>4</sub> used in this work, the optical axis is set coincident with the  $x$ -axis, i.e.,  $K_x = K_c$ ,  $K_y = K_z = K_a$ , where  $K_c$  ( $K_a$ ) is the thermal conductivity parallel (orthogonal) to the optical axis. The temperature distribution in the laser crystal is obtained by solving the coupled initial and boundary problems of parabolic partial differential equations (PDE) of heat conduction Equation (19).

The initial temperature distribution in crystal is equal to environmental temperature  $T_0$ ; therefore, the initial condition is:

$$T(\mathbf{r}, 0) = T_0. \quad (20)$$

Because the convection heat transfer coefficient with air is much smaller than with heat sink [27], we can suppose that the crystals are approximately adiabatic with air at the end faces and have convection heat transfer coefficient  $H$  with heat sink at side faces. The boundary conditions are

$$K_x \frac{\partial T}{\partial x} \Big|_{x=\frac{h}{2}} = H \left[ T_0 - T \left( \frac{h}{2}, y, z \right) \right], \quad (21)$$

$$-K_x \frac{\partial T}{\partial x} \Big|_{x=-\frac{h}{2}} = H \left[ T_0 - T \left( -\frac{h}{2}, y, z \right) \right], \quad (22)$$

$$K_y \frac{\partial T}{\partial y} \Big|_{y=\frac{w}{2}} = H \left[ T_0 - T \left( x, \frac{w}{2}, z \right) \right], \quad (23)$$

$$-K_y \frac{\partial T}{\partial y} \Big|_{y=-\frac{w}{2}} = H \left[ T_0 - T \left( x, -\frac{w}{2}, z \right) \right], \quad (24)$$

$$\frac{\partial T}{\partial z} \Big|_{z=0} = \frac{\partial T}{\partial z} \Big|_{z=l_c} = 0, \quad (25)$$

where  $w$  and  $h$  are width and height of crystal. Then, according to our SDTI model [23], we can solve the temperature-dependent pump and laser intensity distributions considering coupled thermal effects.

### 3. Experimental Setup

The experimental setup of the dual-rod AO Q-switched resonator is shown in Figure 2. Two identical a-cut  $2 \times 2 \times 25$  mm<sup>3</sup> low doping concentration of 0.5 at.% Nd:YVO<sub>4</sub> crystals water-cooled by copper heat sinks were used as the gain medium. Both end faces of the crystals were dichroic anti-reflective (AR) coated at 1064 nm and 888 nm with transmissivity higher than 99.9% and 98%, respectively. The crystals were pumped at 888 nm ( $^4I_{9/2} \rightarrow ^4F_{3/2}$ ) and lasing at 1064 nm ( $^4F_{3/2} \rightarrow ^4I_{11/2}$ ) as a quasi-three-level system for reducing thermal effect. The dual-rod and dual-end pumped geometry was chosen to enhance the pump power. A symmetrical Z-shape cavity with the AOM at the center for intracavity Q-switching is designed to obtain similar mode matching in both crystals. The AOM is with module of Ante I-QS027-2C4G-U5-ST1. The fiber-coupled laser diode module of nLIGHT NL-P4-110-0888-2-A-R01 with numerical aperture of 0.22 and core diameter of 400  $\mu$ m was used in the experiment as the pump source. The temperature of the laser diode was controlled by the thermoelectric cooling module (TECM) and the center wavelength of the laser diode could be temperature-tuned by adjusting the temperature of the laser diode (LD) with TECM. The dichroic mirrors were AR coated at 888 nm and high-reflective (HR) coated at 1064 nm for lasers at the incidence angle of 22.5° with the transmissivity more than 98% and reflectivity higher than 99.9%, respectively. A set of near aberration-free lenses were used to image the pump mode from the fiber onto the Nd:YVO<sub>4</sub> crystal with the pump waist radius of about  $\omega_{p0} = 450$   $\mu$ m. The pump waist is at a distance of about 1/3 crystal length from the incident end face for each crystal. A symmetric planar-planar resonator was used with the totally reflecting mirror M1 and the output coupler (OC) M2, which has the transmissivity of 57% at 1064 nm. Actually, our resonator is operating as a compound stable cavity due to the thermal compensation management of dual-crystal, which is designed for not only reaching a good mode matching to reach high power but also outputting a stable near TEM<sub>00</sub> mode. The transmissivity of the output coupler is also fully optimized, which is around the maximum output case and cavity stability

cannot be broken. These ideas and designs are referred to in Refs. [1,2]. The parameters used in our numerical simulations are listed in Table 1 corresponding to our experimental systems.

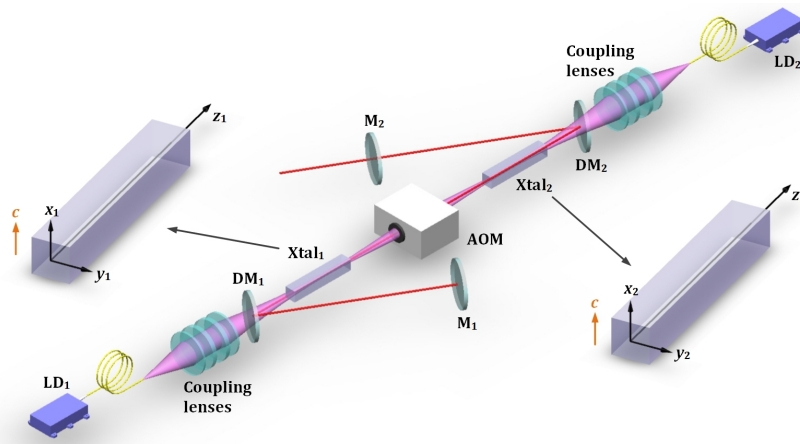


**Figure 2.** Experimental setup of the dual-rod acousto-optic Q-switched laser systems with the corresponding coordinate frames: LD, laser diode; Xtal, crystal; AOM, acoustic optical modulator; M, mirror; DM, dichroic mirror.

**Table 1.** The parameters used in this work.

Symbol	Value (Ref.)	Symbol	Value (Ref.)
$\lambda_p$	888 nm	$T_0$	298 K (25 °C)
$\lambda_s$	1064 nm	$K_a$	5.10 W/(mK) [16]
$\lambda_f$	1032 nm [6]	$K_c$	5.23 W/(mK) [16]
$l$	63 cm	$\rho$	4.22 g/cm <sup>3</sup> [16]
$l_m$	6 cm	$C_p$	0.56 J/(gK) [16]
$l_c$	2.5 cm	$H$	$2 \times 10^4$ Wm <sup>2</sup> K [27]
$w$	2 mm	$\sigma_{ap0}(T_0)$	$1.2 \times 10^{-24}$ m <sup>2</sup> [1]
$h$	2 mm	$\sigma_{es0}(T_0)$	$15.6 \times 10^{-23}$ m <sup>2</sup> [31]
$n_{tot}$	$6.24 \times 10^{25}$ /m <sup>3</sup>	$n_o$	1.96 [32]
$W_{up}$	$0.8 \times 10^{-21}$ m <sup>3</sup> /s [28]	$n_e$	2.17 [32]
$\tau_1$	530 ps [29]	$n_m$	1.45 [25]
$\tau_4$	104.29 $\mu$ s, 0.5% at. [10]	$T_{OC}$	0.57
$\tau_{up}$	20 ns [22]	$L$	0.02
$\beta_{40}$	0.420 [30]	$\delta_0$	0.8 [25]
$\beta_{41}$	0.467 [30]	$t_s$	60 nm [25]
$\beta_{42}$	0.110 [30]	$t_{on}$	5 $\mu$ s
$\beta_{43}$	0.003 [30]	$\omega_0$	420 $\mu$ m
$S$	$10^{-11}$ [22]	$\omega_{p0}$	450 $\mu$ m

The output power of the oscillator was measured by the OPHIR FL250A-LP1-DIF power meter. The SPIRICON M2-200s laser beam analyzer was used to measure the beam quality. In Q-switching operation, the pulse signal was detected by a high-speed silicon photoelectric detector as well as a Tektronix TDS 3202B digital phosphor oscilloscope with 300 MHz bandwidth. The thermal imager (FLIR: T420, TLIR-T62101, with a 320 × 240 imaging resolution) is used to measure the average temperature on the surface of the crystal, the measured data of which is the important guide of our numerical simulations. Because the resolution of our thermal imaging is limited and the crystal is small, it is impossible to measure the detailed temperature distribution. In our experiment, we oriented to the crystal at a tiny angle and adjusted the thermal imaging to a proper measured distance that a resolution area can approximately cover the end face of crystal. The measured temperature is approximately the average temperature at the end surface of crystal within a tolerable error.

### 4. Results and Discussion

#### 4.1. CW Condition

For the steady CW state, time derivative terms in Equations (1)–(6) and Equations (12) and (13) in our theoretical model are zero. The pump and laser power distributions in two Nd:YVO<sub>4</sub> crystals can be simulated with a MATLAB procedure and the numerical results are shown in Figure 3a,b. The intracavity circular laser powers and pumps absorption processes are shown in Figure 3a,b. The input pump power on each crystal is 67 W and the total pump power is 134 W. As can be seen, Xtal 2 undertakes a higher forward laser power than Xtal 1 because it is near the OC. The pump absorptivity in each crystal is approximately equal due to the symmetry of the cavity. The simulated output power is 62.8 W, as can be obtained in Figure 3b, which is in accordance with our experimental result 61.6 W within the scope of tolerable error.

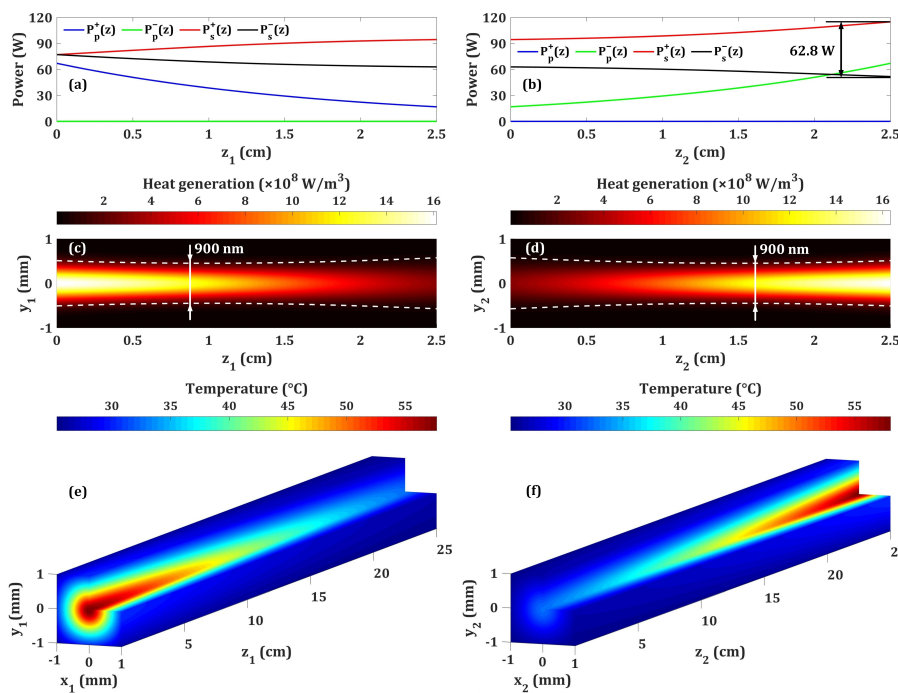


**Figure 3.** Power distributions along the z-axis in (a) Xtal 1; (b) Xtal 2, heat generation distributions of (c) Xtal 1 at face  $x_1 = 0$ ; (d) Xtal 2 at face  $x_2 = 0$  and temperature distributions within (e) Xtal; and (f) Xtal 2 for the continuous-wave condition.

Then, the heat generation can be calculated by using Equations (17) and (18) in our thermal model. The thermal power density and pump waist distributions within each crystal are depicted in Figure 3c,d. The pump waist radius for each crystal is 450 μm at a distance of 1/3 crystal length from the incident end face for each crystal, as can be seen in Figure 3c,d. The profiles of heat generation distribution coincide approximately with the distributions of pump beam.

The steady state temperature distributions obey the heat conduction Equation (19) without the time derivative term while with the spatial boundary conditions Equations (21)–(25). The temperature distributions within the two crystals are show in Figure 3e,f. In the numerical simulation above, we also considered how the interaction effect between spatial temperature and temperature induces cross sections changing by using the dynamic iteration method [23]. The maximum temperature within Xtal 1 is 57.6 °C. The maximum temperature of Xtal 2 is 58.1 °C, which is a little higher than that of Xtal 1. The average temperature of Xtal 1 on the left side and that of Xtal 2 on the right side are 41.2 °C and 41.6 °C, respectively, which coincide approximately with the measured value of about 43.8 °C via thermal imager.

#### 4.2. Q-Switched Condition

For the Q-switched condition, the power distributions in crystals should obey the 4D coupled equations, Equations (1)–(6) and Equations (12) and (13). In addition, because the intracavity round-trip time of light is much larger than the time of pulse producing, the  $z$ -derivative terms have slowly varying functions in comparison with the  $t$ -derivative terms. Thus, the time-dependent principle barely changes with the effective average of spatial intracavity value being taken into account, as Equation (16) described. Similarly, the space-dependent principle also rarely changes with the effective average of temporal intracavity value considered. Figure 4 shows the numerical results of the temporal evolution of population inversion (a,b), heat generation (c,d) and temperature distribution (e,f) along the  $z$ -axis at the 100 kHz Q-switched condition. For clearly observing the pulse sequence, the maximum time domain span is set as 0.15 ms, before which the laser pulse can reach the steady state but the temperature pulsing growth cannot. The numerical results of output laser power pulse evolution are shown in Figure 5 by solving the coupled rate Equations (1)–(6) and Equation (16). The simulated stable peak power is 17.5 kW and pulse width is 35.4 ns, which are corresponding with the measured value 16.2 kW and 37.5 ns within the scope of tolerance. Additionally, the weak parasitic noisy pulses are also simulated as shown in Figure 5, which actually exist and are observed in our experiment.

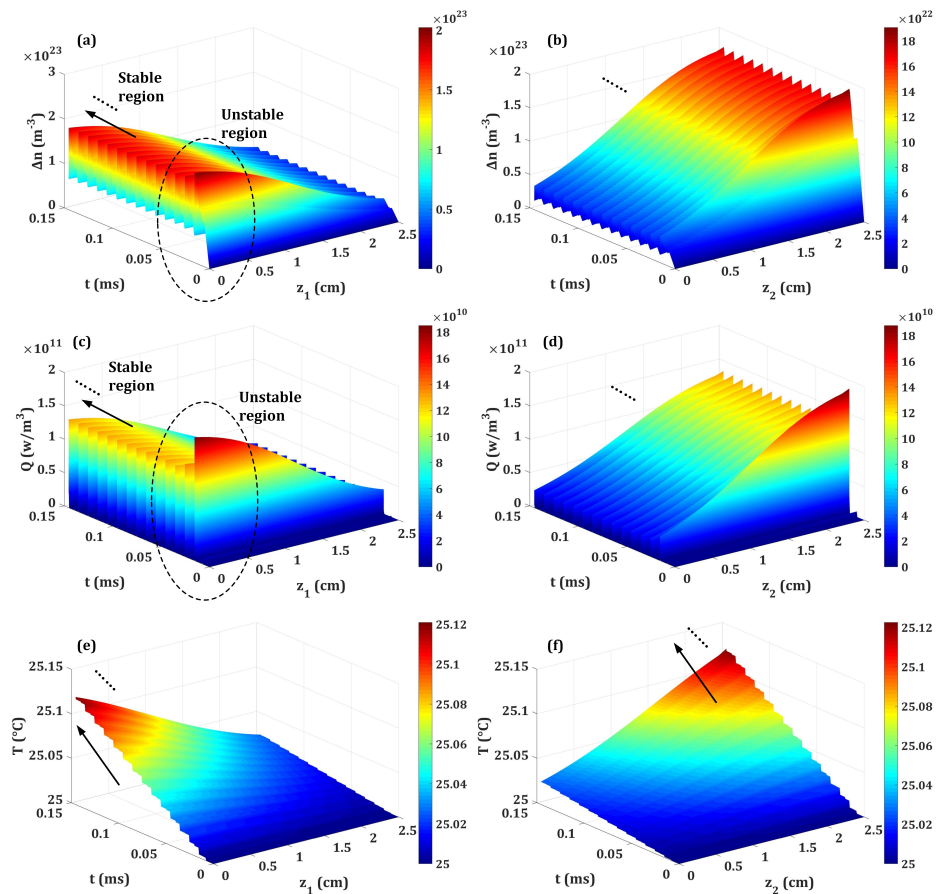


**Figure 4.** The temporal evolution of (a) population inversion in Xtal 1; (b) population inversion in Xtal 2; (c) heat generation in Xtal 1; (d) heat generation in Xtal 2; (e) temperature distribution in Xtal 1; and (f) temperature distribution in Xtal 2 along the  $z$ -axis at 100 kHz Q-switched condition.

In our simulation model, the coupled dynamic equations without any certain periodic function hypotheses are directly solved, calculating thermal power via nonradiative transition rates and energy gaps. Thus, the first few unstable 4D heat generation pluses within two crystals can be solved, as shown in Figure 4c,d, corresponding to the physical reality. To the best of our knowledge,

almost all of previous 4D thermal analysis models [19–21] roughly expressed the thermal load as certain periodic functions using some classical formulas, thus they cannot work out the unstable region, i.e., the first few unstable heat generation periods. The comparison shows an improved accuracy of our new model for simulating 4D heat generation in Q-switched laser crystals. Just like the laser pulse sequence, the heat generation pulses in unstable regions are a mixed train of high-intensity and low-intensity pulses. Figure 4c,d show the temporal evolution of temperature growth in two crystals. After 1.5 ms, the increment of maximum temperature in each crystal is about 0.12 °C, while the temperature distributions do not reach the steady state.

The parasitic sub-pulses, as shown in Figure 5, are usual phenomenon in active Q-switched lasers, the detailed explanation of which can be Referred to Ref. [33]. This unwanted phenomenon can be eliminated by adjusting duty cycle, but the parasitic pulses here are so weak that cannot impact on output properties. Additionally, the existing parasitic pulses can reflect the accuracy of our numerical model. Thus, we did not address it in this work. The experimental pulse duration is 37.5 ns, which is in accordance with the simulation result that 35.4 ns in a tolerable error.

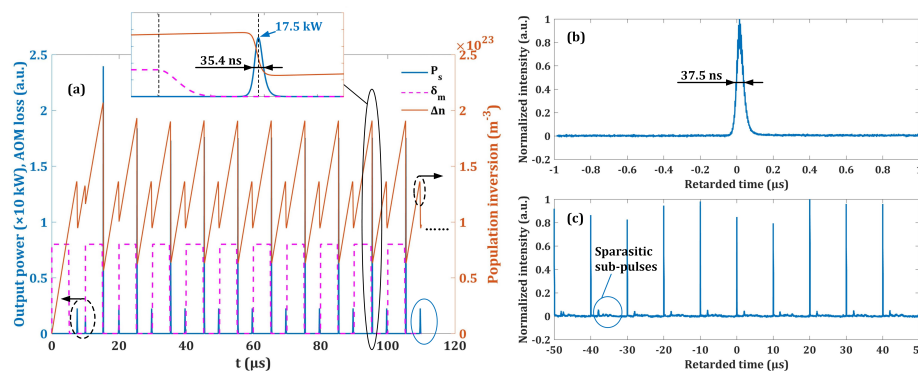


**Figure 5.** (a) simulation of temporal evolution of output laser power, average intracavity population inversion and acoustic-optical modulating loss, and the insert shows the detail of pulse producing. The insert shows the detail of a stable pulse, which is consistent with (b) the experimental measured pulse shape within a tolerable error; (c) the experimental temporal scope trace of output pulse sequence.

### 4.3. Beam Quality

Figure 6 shows the experimental results of output laser beam quality and spatial mode profile measured by our SPIRICON M2-200s laser beam analyzer. The output is near TEM<sub>00</sub> mode with beam quality that  $M_x^2 = 1.113$  and  $M_y^2 = 1.147$  in a stable Q-switched condition. The good measured beam quality verifies that it is proper to make the Gaussian mode assumption in our simulation.

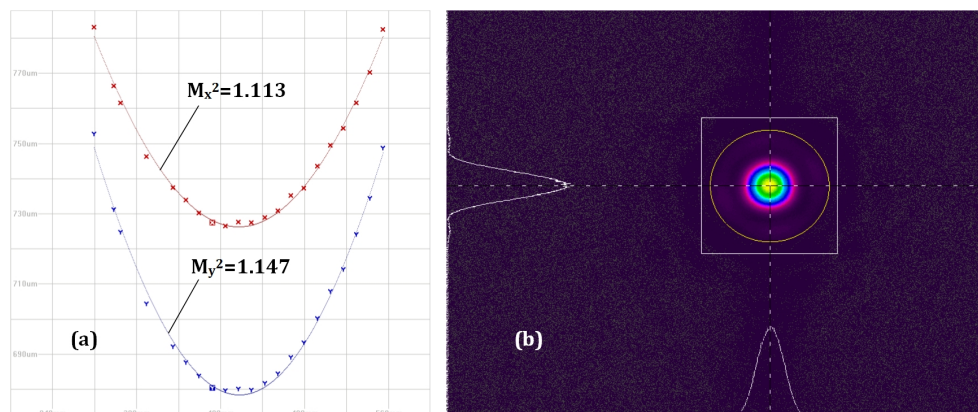


**Figure 6.** (a) experimental output laser beam quality; (b) spatial mode profile measuring via a laser beam analyzer in the stable Q-switched condition.

4.4. Discussion

Through further numerical simulation, only about 1 s is needed for the temperature distributions to yield to convergence after the Q-switched system was turned on. The temporal evolution of maximum temperature in Xtal 1 at CW, 100 kHz Q-switched, 50 kHz Q-switched and nonlaser conditions are shown in Figure 7a.

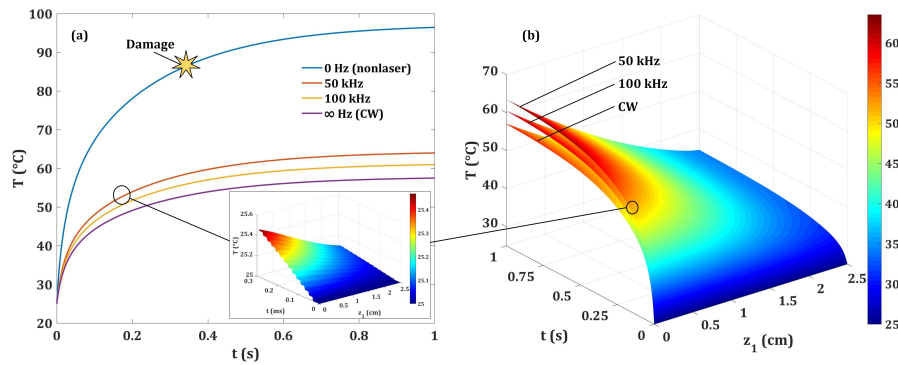


**Figure 7.** The temporal evolution of (a) maximum temperature in Xtal 1 at CW, 100 kHz Q-switched, 50 kHz Q-switched and nonlaser conditions; (b) temperature distribution in Xtal 1 along the z-axis at CW, 100 kHz Q-switched and 50 kHz Q-switched conditions.

The  $(z, t)$ -dependent temperature distributions at CW, 100 kHz Q-switched and 50 kHz Q-switched conditions are shown in Figure 7b. It can be seen that the higher the Q-switched repetition-rate, the lower the thermal effect in crystal and the closer to the CW conditions. The nonlaser condition will cause serious thermal effects and can easily damage the crystal. We also observed this kind of damage under nonlasering conditions in our previous experiment. The main reason is that the temperature under nonlasering conditions is much higher than that of the lasering condition, which was studied in our previous work [23]. More detailed origins and principles about this are referred to in Ref. [34].

Figure 8a shows the simulation results and corresponding experimental data of average output power versus pump powers. Figure 8b shows the simulation results and corresponding measured data of average temperature on the left end face of Xtal 1 versus pump powers. We have considered the compensation of the measurement resolution of the thermal imager in the average method. These comparisons between experimental and numerical results verify the accuracy of our model in both simulating power and thermal effect domain.

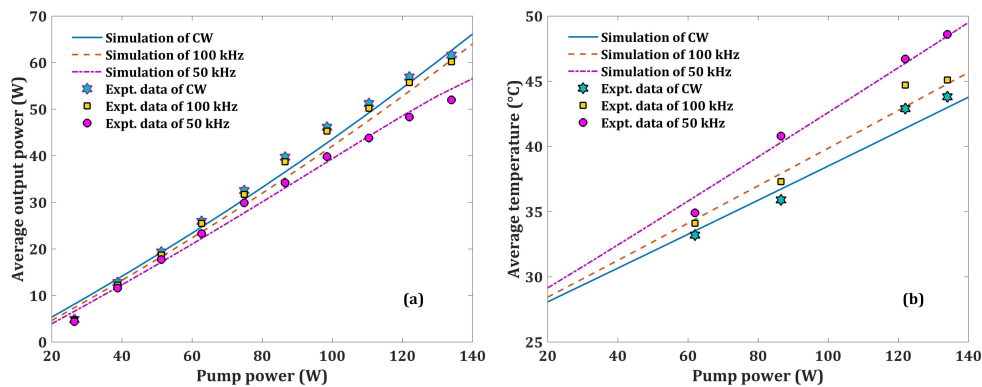


**Figure 8.** The simulation results and corresponding experimental data of (a) average output power; (b) average temperature on the left end face of Xtal 1, versus pump powers at CW, 100 kHz Q-switched and 100 kHz Q-switched conditions.

## 5. Conclusions

In this paper, we built a theoretical model based upon high-power high-efficiency 888 nm in-band pumped Nd:YVO<sub>4</sub> dual-rod CW and AO Q-switched lasers. In addition, an 888 nm in-band pumping scheme effectively deduced quantum defects and compensated for the deleterious thermal effects. A compound symmetrical thermal stable cavity is designed for not only reaching good mode matching to reach high power but also outputting a stable near TEM<sub>00</sub> mode with beam quality that  $M_x^2 = 1.113$  and  $M_y^2 = 1.147$ . Moreover, the investigations of the corresponding space-time-independent 4D analysis model are also made. Complex physical processes like GSD, fluorescence branching, ETU and CR are included and the coupled effect of thermal effect and temperature-dependent cross sections are considered in our model. By our model, we can accurately simulate the 4D evolution of power, population and temperature distributions in crystals at CW and different repetition-rate conditions. Our model can solve the 4D heat generation evolution in not only the steady pulse region but also the unstable region at the beginning. Our results show that the higher the Q-switched repetition-rate, the lower the thermal effect in crystal and the closer to the CW conditions, which is corresponding with the experiment experience and physical reality. The simulated output properties and temperature principles are in good agreement with the experimental results. Our theoretical model can also be further applied in multi-rod or other Q-switched laser systems with complex cavity types for instruction power upgrade and laser machining application.

**Author Contributions:** Y.S. proposed the theoretical model, W.Z. and M.G. conceived and designed the experiments; W.Z. performed the experiments; Y.S. and Y.W. analyzed the data; M.G. and X.F. contributed materials; Y.S. and Y.M. wrote the paper.

**Conflicts of Interest:** The authors declare no conflict of interest.

## References

- McDonagh, L.; Wallenstein, R.; Knappe, R.; Nebel, A. High efficiency 60 W TEM<sub>00</sub> Nd:YVO<sub>4</sub> oscillator pumped at 888 nm. *Opt. Lett.* **2006**, *31*, 3297–3299.
- McDonagh, L.; Wallenstein, R.; Nebel, A.; Knappe, R. 888 nm pumping of Nd:YVO<sub>4</sub> for high-power high-efficiency TEM<sub>00</sub> lasers. *SPIE Proc.* **2007**, *6451*, 64510F.
- Hong, H.L.; Huang, L.; Liu, Q.; Yan, P.; Gong, M.L. Compact high-power, TEM<sub>00</sub> acousto-optics Q-switched Nd:YVO<sub>4</sub> oscillator pumped at 888 nm. *Appl. Opt.* **2012**, *51*, 323–327.
- McDonagh, L.; Wallenstein, R.; Nebel, A. 111 W, 110 MHz repetition-rate, passively mode-locked TEM<sub>00</sub> Nd:YVO<sub>4</sub> master oscillator power amplifier pumped at 888 nm. *Opt. Lett.* **2007**, *32*, 1259–1261.
- Nadeau, M.C.; Petit, S.; Balcou, P.; Czarny, R.; Montant, S.; Simon-Boisson, C. Picosecond pulses of variable duration from a high-power passively mode-locked Nd:YVO<sub>4</sub> laser free of spatial hole burning. *Opt. Lett.* **2010**, *35*, 1644–1646.
- Délen, X.; Balembois, F.; Georges, P. Design of a high gain single stage and single pass Nd:YVO<sub>4</sub> passive picosecond amplifier. *J. Opt. Soc. Am. B* **2012**, *29*, 2339–2346.
- Luhrmann, M.; Theobald, C.; Wallenstein, R.; L’huillier, J.A. High energy cw-diode pumped Nd:YVO<sub>4</sub> regenerative amplifier with efficient second harmonic generation. *Opt. Express* **2009**, *25*, 22761–22766.
- McDonagh, L.; Wallenstein, R. Low-noise 62 W CW intracavity-doubled TEM<sub>00</sub> Nd:YVO<sub>4</sub> green laser pumped at 888 nm. *Opt. Lett.* **2007**, *32*, 802–804.
- Schäfer, C.; Fries, C.; Theobald, C.; L’huillier, J.A. Parametric Kerr lens mode-locked, 888 nm pumped Nd:YVO<sub>4</sub> laser. *Opt. Lett.* **2011**, *36*, 2674–2676.
- Huang, Z.Y.; Huang, Y.D.; Chen, Y.J.; Luo, Z.D. Theoretical study on the laser performances of Nd<sup>3+</sup>:YAG and Nd<sup>3+</sup>:YVO<sub>4</sub> under indirect and direct pumping. *J. Opt. Soc. Am. B* **2005**, *22*, 2564–2569.
- Graf, T.; Balmer, J.E.; Weber, R.; Weber, H.P. Multi-Nd:YAG-rod variable-configuration resonator (VCR) end pumped by multiple diode-laser bars. *Opt. Commun.* **1997**, *135*, 171–178.
- Driedger, K.P.; Ifflander, R.M.; Weber, H. Multirod Resonators for High-Power Solid-state Lasers with Improved Beam Quality. *IEEE J. Quantum Electron.* **1988**, *24*, 665–674.

13. Yan, X.P.; Liu, Q.; Fu, X.; Chen, H.L.; Wang, D.S.; Gong, M.L. Comparative investigation on performance of acoustooptically Q-switched dual-rod Nd:YAG-Nd:YVO<sub>4</sub> laser and dual-rod Nd:YVO<sub>4</sub>-Nd:YVO<sub>4</sub> laser. *Appl. Opt.* **2010**, *49*, 4131–4138.
14. Yan, X.P.; Liu, Q.; Fu, X.; Chen, H.L.; Gong, M.L.; Wang, D.S. High repetition rate dual-rod acousto-optics Q-switched composite Nd:YVO<sub>4</sub> laser. *Opt. Express* **2009**, *17*, 21956–21968.
15. Song, J.; Li, C.; Ueda, K. Thermal influence of saturable absorber in passively Q-switched diode-pumped cw Nd:YAG/Cr<sup>4+</sup>:YAG laser. *Opt. Commun.* **2012**, *177*, 155–160.
16. Zhang, S.Y.; Wang, X. Thermal model of continuous-wave end-pumped passively Q-switched laser. *Opt. Commun.* **2013**, *295*, 155–160.
17. Li, S.X.; Li, Y.F.; Zhao, S.Z.; Li, G.Q.; Wang, X.M.; Yang, K.J.; Li, D.C.; Li, T. Thermal effect investigation and passively Q-switched laser performance of composite Nd:YVO<sub>4</sub> crystals. *Opt. Laser Technol.* **2015**, *68*, 146–150.
18. Wang, S.; Eichler, H.J.; Wang, X.; Kallmeyer, F.; Ge, J.; Riesbeck, T.; Chen, J. Diode end pumped Nd:YAG laser at 946 nm with high pulse energy limited by thermal lensing. *Appl. Phys. B* **2009**, *95*, 721–730.
19. Li, T.; Zhang, S.Y.; Zhao, S.Z.; Yang, K.J.; Zhuo, Z. Thermal modeling of the continuous-wave end-pumped Q-switched lasers. *Opt. Commun.* **2010**, *283*, 3070–3075.
20. Guy, S.; Bonner, C.L.; Shepherd, D.P.; Hanna, D.C.; Tropper, A.C.; Ferrand, B. High-Inversion Densities in Nd:YAG: Upconversion and Bleaching. *IEEE J. Quantum Electron.* **1998**, *34*, 900–909.
21. Chen, X.Y.; Wu, J.; Wu, C.T.; Sun, H.T.; Yu, Y.J.; Jin, G.Y. Analysis of thermal effects in a pulsed laser diode end pumped single-ended composite Tm:YAG laser. *Laser Phys.* **2015**, *25*, 045003.
22. Pollnau, M.; Hardman, P.J.; Kern, M.A.; Clarkson, W.A.; Hanna, D.C. Upconversion-induced heat generation and thermal lensing in Nd:YLF and Nd:YAG. *Phys. Rev. B* **1998**, *58*, 16076–16092.
23. Shen, Y.J.; Gong, M.L.; Ji, E.C.; Fu, X.; Sun, L.C. Spatial dynamic thermal iteration model for 888 nm end-pumped Nd:YVO<sub>4</sub> solid-state laser oscillators and amplifiers. *Opt. Commun.* **2017**, *383*, 430–440.
24. Eichhorn, M. Quasi-three-level solid-state lasers in the near and mid infrared based on trivalent rare earth ions. *Appl. Phys. B* **2008**, *93*, 269–316.
25. Li, D.C.; Zhao, S.Z.; Li, G.Q.; Yang, K.J. Optimization of peak power of doubly Q-switched lasers with both an acousto-optic modulator and a Cr<sup>4+</sup>-doped saturable absorber. *Appl. Opt.* **2006**, *45*, 5767–5776.
26. Wang, X.S.; Song, J.; Sun, H.; Xu, Z.Z.; Qiu, J.R. Multiphoton-excited upconversion luminescence of Nd:YVO<sub>4</sub>. *Opt. Express* **2007**, *15*, 1384–1389.
27. Weber, R.; Neuenschwander, B.; Weber, H.P. Thermal effects in solid-state laser materials. *Opt. Mater.* **1999**, *11*, 245–254.
28. Yoon, S.J.; Yan, R.P.; Stephen, J.B.; Jacob, I.M. Energy transfer upconversion measurements for popular neodymium-doped crystals. *SPIE Proc.* **2015**, *9342*, 93421D.
29. Bibeau, C.; Stephen, A.P.; Howard, T.P. Direct measurements of the terminal laser level lifetime in neodymium-doped crystals and glasses. *J. Opt. Soc. Am. B* **1995**, *12*, 1981–1992.
30. Lomheim, T.S.; DeShazer, L.G. Optical-absorption intensities of trivalent neodymium in the uniaxial crystal yttrium orthovanadate. *J. Appl. Phys.* **1978**, *49*, 5517–5522.
31. Sato, Y.; Taira, K. Temperature dependencies of stimulated emission cross section for Nd-doped solid-state laser materials. *Opt. Express* **2012**, *2*, 1076–1087.
32. Tung, J.C.; Wu, T.Y.; Liang, H.C.; Chen, Y.F. Precise measurement of the thermo-optical coefficients of various Nd-doped vanadates with an intracavity self-mode-locked scheme. *Laser Phys.* **2014**, *24*, 035804.
33. Koehner, W. *Solid-State Laser Engineering*, 6th ed.; Springer: New York, NY, USA, 2006.
34. Shen, Y.; Bo, Y.; Zong, N.; Guo, Y.D.; Peng, Q.J.; Li, J.; Pan, Y.B.; Zhang, J.Y.; Cui, D.F.; Xu, Z.Y. Experimental and Theoretical Investigation of Pump Laser Induced Thermal Damage for Polycrystalline Ceramic and Crystal Nd:YAG. *IEEE J. Sel. Top. Quantum Electron.* **2015**, *21*, 900–909.

